



# Structural Characteristics and Electric and Magnetic Features of the $\text{Nd}_{2.68}\text{Sr}_{1.32}\text{Mn}_{1.2}\text{Ti}_{1.32}\text{Fe}_{1.48}\text{O}_{12}$ Ferromagnetic Semiconductor

J. A. Cuervo Farfán<sup>1</sup> · J. P. Benavides Lara<sup>1</sup> · C. A. Parra Vargas<sup>2</sup> ·  
D. A. Landínez Téllez<sup>1</sup> · J. Roa-Rojas<sup>1</sup> 

Received: 2 July 2020 / Accepted: 12 September 2020 / Published online: 26 September 2020  
© Springer Science+Business Media, LLC, part of Springer Nature 2020

## Abstract

The inclusion of several cations in the A and B crystallographic sites of the  $\text{A}_{4-x}\text{A}'_x\text{B}_{4-y-z}\text{B}'_y\text{B}''_z\text{O}_{12}$  complex perovskite gives rise to diverse physical properties, depending on the constituent elements of the material. In this work, structural, morphological, compositional, magnetic and electric characterization of the solid-reacted compound  $\text{Nd}_{2.68}\text{Sr}_{1.32}\text{Mn}_{1.2}\text{Ti}_{1.32}\text{Fe}_{1.48}\text{O}_{12}$  is reported. Rietveld analysis of X-ray diffraction data revealed that this material crystallizes in an orthorhombic perovskite structure (*Pnma*, #62, space group). The surface morphologic study showed the formation of polycrystalline material with diverse shape of grains of 1.50  $\mu\text{m}$  mean size. Compositional characterization through the energy-dispersive X-ray spectroscopy technique suggests that there are no other elements in the material besides the expected Nd, Sr, Mn, Ti, Fe and O, which are present in percentage proportions very close to the expected values from the material stoichiometry. E–J curves exhibit hysteretic features which are typical of the thermistor-like materials. Electric resistivity as a function of temperature showed an Arrhenius behavior also observed in doped semiconductors. Diffuse reflectance spectra revealed an optical band gap of 1.17 eV. Magnetic susceptibility measurements as a function of temperature evidenced a ferrimagnetic response, and hysteretic curves of magnetization at  $T = 50$  K, 200 K and 300 K corroborated the occurrence of magnetic ordering, which permit to classify this material as a ferrimagnetic semiconductor with potential applicability in the spintronic device industry at room temperature.

**Keywords** Perovskite · Crystalline and granular microstructure · Magnetic response · Electric characteristics

---

✉ J. Roa-Rojas  
jroar@unal.edu.co

<sup>1</sup> Grupo de Física de Nuevos Materiales, Departamento de Física, Universidad Nacional de Colombia, 5997 Bogotá, DC, Colombia

<sup>2</sup> Grupo Física de Materiales, Escuela de Física, Universidad Pedagógica y Tecnológica de Colombia, Tunja, Colombia

## 1 Introduction

With the emergence of spintronics, the magnetic media information storage industry evolved dramatically due to the possibility of minimizing ferromagnetic domains and manipulating their individual spins, allowing progress in optimizing extremely relevant factors such as processing speed and the increase in the capacity of data stored per unit volume of the material used as a memory device [1]. In this context, magnetic semiconductors play a very important role because their multifunctional properties and the interplay between them substantially increase their potential applicability in nanoelectronic and spintronic systems. Ferromagnetism is expected in metallic-type materials in which the exchange mechanisms are theoretically explainable, while semiconductivity is usually more associated with dielectric than metallic behavior, which is why the occurrence of the two behaviors in a single material constitutes a type of exotic magnetic response, as can be seen in its observation in materials that show extraordinary properties such as colossal magnetoresistance, which is typical of materials known as manganites [2], belonging to a group of ceramics called perovskites [3].

These ceramic oxide materials have a simple form of cubic structure with the ideal formula  $ABO_3$ , which allows obtaining a large number of possible compositions because rare earth and alkaline earth may be included in sites A of the structure and both rare earths and a wide variety of transition metals and semi-metals may be included in sites B. Depending on the properties of the substitute elements at crystallographic sites A and B, the perovskite structure can adopt various spatial groups and suffer distortions in  $BO_6$  octahedra, which strongly influence the physical properties of the material [4, 5]. When multiple cations are used at site A or B, these materials are called complex perovskites and the structure may assume an ordered arrangement of the cations known as a superstructure or a distribution of cationic disorder, which also affects their optical, electrical and magnetic behaviors.

Although the most studied complex perovskite is  $A_2BB'O_6$  [6], in which it is possible to obtain the order of cations B and B' alternately throughout the structure, there is another, less studied complex but with the same possibility of affecting physical properties by modifying the chemical composition. It is the double perovskite  $AA'B_2O_6$  usually identified as  $A_2A'B_4O_{12}$  to achieve integer occupation of its components in the structure. Although in this group of perovskites a cooperative balance is eventually achieved between octahedral inclinations and distortions due to the Jahn–Teller effect [7], in most cases they present cationic disorder at sites A and A'. Furthermore, its probability of crystallization largely depends on the proximity between their ionic radius values, a fact that favors their growth in space groups expected for simple perovskites such as  $Pnma$  (#62) and its corresponding subgroups [8].

In the search for new perovskite-type materials with useful magnetic and electrical properties in today's nanoelectronics industry, a practice that has shown good results has to do with enthronement of various separate material components in the synthesis of a single material [9]. It is well known that orthoferrites

and rare earth-based manganites show multiferroic properties, even though these two groups of perovskites show structural differences between them [10, 11]. While the former crystallize into orthorhombic structures (space group  $Pbnm$ , #62), the latter tend to form a rhombohedral structure (space group  $R-3c$ , #167) [12], with reports of orthorhombic structure [13] and even cubic [14], depending on the processes of synthesis and analysis techniques. On the other hand, the dielectric properties of  $\text{SrTiO}_3$  have been well known for decades [15]. With the aim of finding a combination of physical properties related to the previous materials, in this work the  $\text{Nd}_{2.68}\text{Sr}_{1.32}\text{Mn}_{1.2}\text{Ti}_{1.32}\text{Fe}_{1.48}\text{O}_{12}$  perovskite-like compound (with generic formula  $\text{A}_{4-x}\text{A}'_x\text{B}_{4-y-z}\text{B}'_y\text{B}''_z\text{O}_{12}$ ) is proposed, to which studies of the crystalline structure, the electrical response and the magnetic characteristic have been carried out, finding it behaves like a ferrimagnetic semiconductor.

## 2 Materials and Methods

The procedure used in the production of  $\text{Nd}_{2.68}\text{Sr}_{1.32}\text{Mn}_{1.2}\text{Ti}_{1.32}\text{Fe}_{1.48}\text{O}_{12}$  samples was the standard solid-state reaction technique, from high-purity precursor oxides supplied by Sigma-Aldrich:  $\text{Nd}_2\text{O}_3$  (99.9%),  $\text{SrCO}_3$  (99.98%),  $\text{Mn}_2\text{O}_3$  (99.9%),  $\text{TiO}_2$  (99.99%) and  $\text{Fe}_2\text{O}_3$  (99.9%). Once the stoichiometric masses of the formula were determined by means of an analytical balance with precision 0.1 mg, the powdered oxides were mixed in an agate mortar for an uninterrupted time of 2 h. Subsequently, the obtained mixture was subjected to a calcination process in a Lindberg Blue tube furnace at a temperature of 1080 °C for 48 h. The calcined material was moistened in acetone and ground again for 30 min, after which it was die-cut for 15 min, under a pressure of 480 MPa, giving the samples the shape of pellets 9.0 mm in diameter and 1.5 mm in thickness. Subsequently, the samples were brought to 1200 °C for the final sintering thermal process for 72 h, to guarantee the grain growth process and the densification of the samples. The structural characterization of the samples was carried out using a PANalytical X'pert Pro X-ray diffractometer, applying the Bragg–Brentano configuration, with a gradual step of 0.001° in 2 $\theta$  by  $t = 10$  s, using a  $\text{CuK}_\alpha$  X-ray tube with  $\lambda = 1.540598$  Å. The obtained data were analyzed by means of rigorous Rietveld refinement. The surface morphological study of the samples was carried out by means of scanning electron microscopy (SEM) images taken on a TESCAN Vega 3 SB equipment with backscatter (BSE) and secondary (SE) detectors. Using an X-ray cannon microprobe (Bruker) attached to the electron microscope, a semiquantitative energy-dispersive spectroscopy (EDS) analysis was performed to determine the composition of the samples. The electrical response was measured on 5.0-mm-long, 2.0-mm-wide and 1.0-mm-thick rectangular samples cut with a diamond disk, on which gold electrodes were deposited. The electrical resistivity measurements were made in the temperature regime between 50 and 425 K in a Janis Research cryogenic system (VPF-475) with temperature variation through a Lake Shore 332 controller, at a rate of 1.5 K/min. I–V characteristics at room temperature were obtained by using a Keithley-6517A DC electrometer containing a specimen holder with gold-plated silver contacts. Measurements of relative electrical permittivity as a function of frequency at room temperature were made using

an Agilent 4294A frequency analyzer. The band gap and energy excitation regimes at room temperature were examined by using a VARIAN Cary 5000 UV–Vis–NIR diffuse reflectance spectrophotometer, which has an integration sphere with a PMT/Pbs detector. Magnetic characterization took place by means of magnetic susceptibility measurements as a function of temperature (between 50 and 320 K), following the Zero Field Cooling (ZFC) and Field Cooled (FC) recipes in an applied field of 500 Oe, thus as magnetization curves as a function of applied field intensity ( $-8.0$  kOe  $< H < +8.0$  kOe) at the fixed temperatures of 50, 200 and 300 K, using a VSM-VersaLab Quantum Design.

### 3 Analysis, Results and Discussion

#### 3.1 Crystal Structure and Morphology

The result of an exhaustive refinement of the diffraction pattern for the  $\text{Nd}_{2.68}\text{Sr}_{1.32}\text{Mn}_{1.2}\text{Ti}_{1.32}\text{Fe}_{1.48}\text{O}_{12}$  material by means of the GSAS code [16] is presented in Fig. 1. There, the data obtained from the XRD experiment are represented by the symbols, while the solid line corresponds to the theoretical diffractogram, and the difference between the simulated and experimental patterns is shown by another line below the background.

It is concluded from the Rietveld analysis that the obtained material  $\text{Nd}_{2.68}\text{Sr}_{1.32}\text{Mn}_{1.2}\text{Ti}_{1.32}\text{Fe}_{1.48}\text{O}_{12}$  adopts an orthorhombic crystal structure of the complex perovskite type ( $Pnma$  space group, #62), which is characterized by distortions of the  $\text{MnO}_6$ ,  $\text{TiO}_6$  and  $\text{FeO}_6$  octahedra, which are given by the Glazer notation

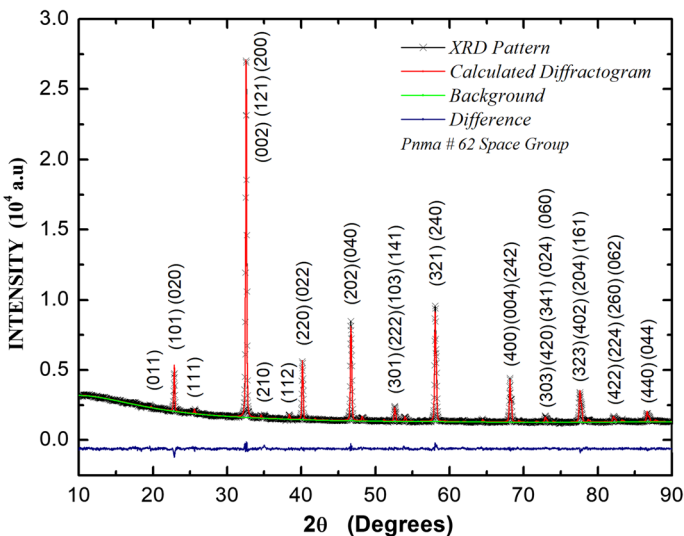


**Fig. 1** Refined XRD pattern for the  $\text{Nd}_{2.68}\text{Sr}_{1.32}\text{Mn}_{1.2}\text{Ti}_{1.32}\text{Fe}_{1.48}\text{O}_{12}$  perovskite. Miller indices corresponding to the diffraction planes are indicated in the figure (Color figure online)

$a^-b^+a^-$ . In this primitive structure, the octahedrons rotate out of phase along the crystallographic  $a$ - and  $c$ -axes and in-phase along the  $b$ -axis. A particularity of this complex perovskite is that the space group  $Pnma$  is expected for simple perovskites of the  $ABO_3$  type, but in this case the crystallization of the complex perovskite occurs in this structure because in the cell there is indistinguishability between the Nd and Sr cations that occupy the sites A outside the octahedra and between de ions Mn, Ti and Fe that are located in the octahedral sites B.

Refinement data with reliability parameters  $\chi^2=2,624$  (Chi-squared),  $R_F^2=4.65\%$  (structure unweighted factor),  $R_{exp}=2.21\%$  (expected R-factor) and  $R_{wp}=3.58\%$  (weighted profile R-factor) resulted in the lattice constants  $a=5.5007 \text{ \AA}$ ,  $b=7.7735 \text{ \AA}$  and  $c=5.5059 \text{ \AA}$ . From these parameters, it is inferred that the resulting orthorhombic structure contains axes  $a$  and  $c$  with values very close to each other, corresponding to 70% of the elongated value of the crystallographic  $b$ -axis. The specific Wyckoff positions of each of the ions in the unit cell are shown in Table 1, where oxygen ions with  $O_1$  notation are sited along the primitive  $b$ -axis, while  $O_2$  anions are found in the  $a$ - $c$  basal plane of the structure. Deviations relative to the ideal Wyckoff positions are an indication of the occurrence of structural distortions, which is expected due to differences between the inherent properties of cations occupying the same crystallographic sites, such as Nd and Sr in the A sites and Mn, Ti and Fe cations in the B sites of the fundamental perovskite. With respect to the notation of the Wyckoff positions, in the table,  $b$ ,  $c$  and  $d$  represent the so-called Wyckoff letters, related to all  $x$ -points for which the possible symmetry groups of each cell site correspond to conjugate subgroups of the  $Pnma$  space group [17].

As shown in Table 1, there are differences between Wyckoff positions for the same element, which constitutes the second factor indicative of a marked structural distortion. The density reported in Table 1 corresponds to the mass of the cell divided by the volume that was calculated from the lattice parameters.

Further evidence of the strong structural distortions of the material is exemplified in Fig. 2a, b, where it is clear that the  $MnO_6$ ,  $TiO_6$  and  $FeO_6$  octahedra suffer in-phase tilting along the crystallographic  $b$  axis and out of phase along the  $a$ - and  $c$ -axes. Furthermore, in Fig. 2c, d, it is possible to see that the distances of the  $O_1$ -B- $O_1$  and  $O_2$ -B- $O_2$  octahedral links differ substantially from each other, also depending on the axis along which these links are found. The same occurs with the octahedral bond angles B- $O_1$ -B and B- $O_2$ -B, which show significant differences. It should be noted that the present analysis considers the indistinguishability between the cations A (Nd and Sr), as well as between the ions B

**Table 1** Wyckoff atomic positions refined for the  $Nd_{2.68}Sr_{1.32}Mn_{1.2}Ti_{1.32}Fe_{1.48}O_{12}$  material

Atom	Wyckoff site	Atomic coordinates		
		$x$	$y$	$z$
Nd, Sr	4c	0.5180(1)	0.2500	0.5047(3)
Mn, Ti, Fe	4b	0.5000	0.0000	0.0000
$O_1$	4c	-0.0069(4)	0.2500	0.4406(2)
$O_2$	8d	0.2789(2)	0.0297(2)	0.7203(5)

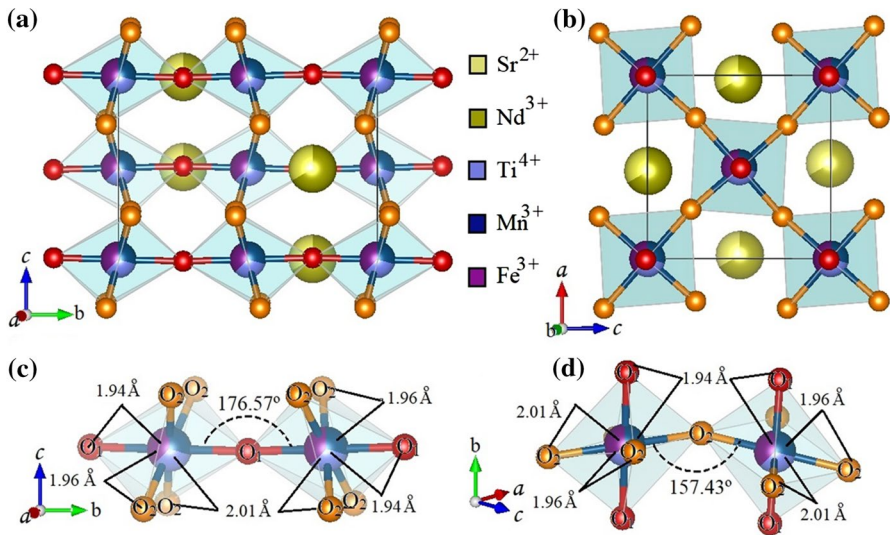


**Fig. 2** Structure of the  $\text{Nd}_{2.68}\text{Sr}_{1.32}\text{Mn}_{1.2}\text{Ti}_{1.32}\text{Fe}_{1.48}\text{O}_{12}$  complex perovskite in the  $bc$ -plane **a** and  $ac$ -plane **b**,  $\text{B}-\text{O}_2-\text{B}$  atomic bond **c** and  $\text{B}-\text{O}_1-\text{B}$  atomic bond **d**, where  $\text{B}=\text{Mn}, \text{Ti}, \text{Fe}$  (Color figure online)

(Mn, Ti and Fe) in the ideal perovskite  $\text{ABO}_3$ , which is another factor that must include distortions in the crystalline cell.

The surface morphology of the samples is exemplified in Fig. 3 of secondary electron SEM images for 17.5 kX (a) and 35 kX (b) increases under the application of a potential difference of 15 kV. The surface shows a porous granular distribution, composed of grains of various shapes and sizes, which have well-defined edges and limited intergranular diffusivity. Although at first glance it is not possible to determine the average grain size, no spurious phases are observed due to unreacted precursor oxides or to compositions that are different from those that constitute the majority structural phase. A dimensional study of the various grains of the images using ImageJ [18] software revealed an average size of 1.50  $\mu\text{m}$ . The nonuniformity of shapes and sizes of grains, the total nondensification, the grain boundaries and the occurrence of porosity will have an impact on the electrical transport properties, as will be evaluated later.

The composition of the material was examined through semiquantitative analysis from the deconvolution of EDS spectra obtained by incising the X-ray microprobe on various specific areas of the samples. The resulting spectrum is shown in Fig. 4, and the percentages of mass obtained are compared with those calculated from the stoichiometric formula, as shown in Table 2.

From the results, it can be concluded that the material does not contain phases corresponding to impurities or elements other than those expected from the composition of the formula  $\text{Nd}_{2.68}\text{Sr}_{1.32}\text{Mn}_{1.2}\text{Ti}_{1.32}\text{Fe}_{1.48}\text{O}_{12}$ . According to the values in Table 2, the experimental and theoretical percentages of mass agree 98%, which is a good indication of obtaining a single crystallographic phase in the samples.

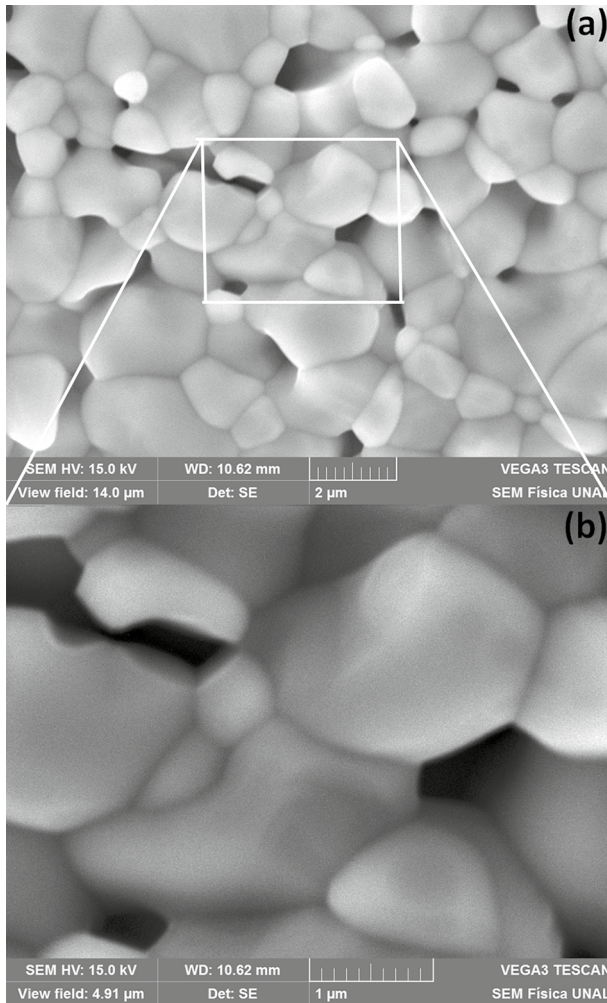


**Fig. 3** Surface morphology of the  $\text{Nd}_{2.68}\text{Sr}_{1.32}\text{Mn}_{1.2}\text{Ti}_{1.32}\text{Fe}_{1.48}\text{O}_{12}$  material obtained from secondary electrons for 17.5 kX **a** and 35 kX **b** magnification

### 3.2 Electrical Response

The characteristic E–J curve shown in Fig. 5 for the  $\text{Nd}_{2.68}\text{Sr}_{1.32}\text{Mn}_{1.2}\text{Ti}_{1.32}\text{Fe}_{1.48}\text{O}_{12}$  exhibits a nonlinear behavior of the varistor diode type with evidences of hysteresis due to the eventual formation of dipolar moments. As the applied current density increases, the polarization field reaches a maximum and decreases, adopting an asymptotic behavior, in the same way as in a P–N-type diode in the direct polarization configuration. Then, as the applied current density decreases, the polarization field is smaller, giving rise to a behavior of hysteretic type. The granular morphological distribution and inhomogeneous diversity of grain sizes, shapes and

**Fig. 4** EDS spectrum analyzed to obtain composition for the  $\text{Nd}_{2.68}\text{Sr}_{1.32}\text{Mn}_{1.2}\text{Ti}_{1.32}\text{Fe}_{1.48}\text{O}_{12}$  complex perovskite (Color figure online)

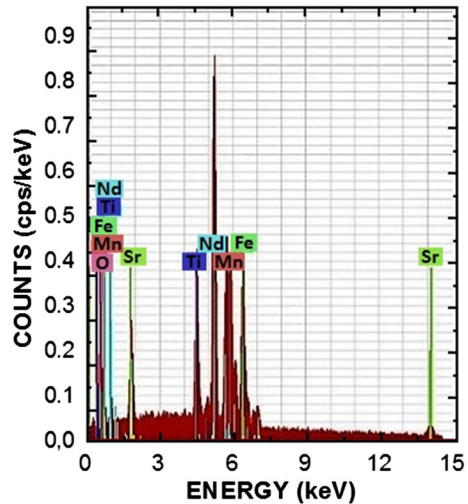


**Table 2** Comparison between stoichiometric and EDS mass percentages for the  $\text{Nd}_{2.68}\text{Sr}_{1.32}\text{Mn}_{1.2}\text{Ti}_{1.32}\text{Fe}_{1.48}\text{O}_{12}$  perovskite

Atom	Theor. mass (%)	Exper. mass (%)
Nd	42.67	43.54
Sr	12.77	13.03
Mn	7.28	7.47
Ti	6.97	7.15
Fe	9.12	9.30
O	21.19	19.51

orientations, as well as the Schottky barriers formed at grain boundaries, are likely to contribute substantially to nonlinear behavior in the E–J response curve [19]. These barriers can be considered as microjunctions between neighboring grains, so that the electrical response for two of these grains is schematized as two consecutive diodes separated by a grain border, which can include pores, idealized as combinations of capacitive and resistive elements, producing E–J responses as expected in varistor diodes [20]. For this reason, the modeling of microstructural electrical transport is carried out using equivalent electrical circuits that contain capacitive and resistive elements, which represent the intragranular and intragranular transport currents in the material [21].

In the low-current-density regime, the I–V curve has a behavior that adjusts with the figure of merit of the varistor, given by

$$I = cV^\alpha, \quad (1)$$

where  $c = 1.78 \times 10^{-4}$  represents a constant and  $\alpha = 1.03 \pm 0.01$  is the known varistor nonlinear coefficient [22]. The nonlinear coefficient presents a value close to unity, showing that at low current densities ( $< 0.4 \text{ mA/cm}^2$ ) the quasi-metallic resistive



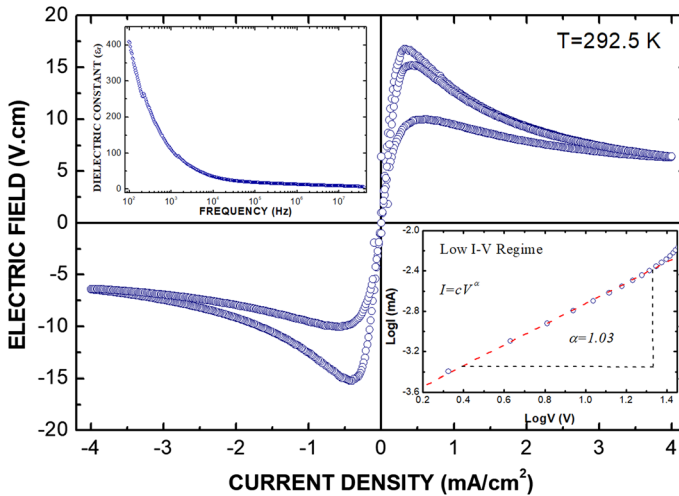


**Fig. 5** E–J hysteric curve obtained for  $\text{Nd}_{2.68}\text{Sr}_{1.32}\text{Mn}_{1.2}\text{Ti}_{1.32}\text{Fe}_{1.48}\text{O}_{12}$  at  $T=292.5$  K. The lower right inset corresponds to the fitting of the data with the varistor figure of merit under the application of low current densities, while the upper left inset represents the relative electrical permittivity as a function of the frequency measured at room temperature. The black arrow indicates the start of the measurement, and the red arrows mark the path followed in the variation in the applied current (Color figure online)

character prevails. As the applied current density increases, the nonohmic dominant effects become more complex because current must flow through semiconductor junctions of coupled grains by inhomogeneities of a morphological nature [23].

The upper left inset in Fig. 5 represents the measurement of the relative dielectric constant for the material. At low frequencies (100 Hz), the dielectric constant has a value of  $\epsilon_r=410$ . However, the  $\epsilon_r$  value falls dramatically with increasing frequency in the range between 100 Hz and 10 kHz. Subsequently, the value of  $\epsilon_r$  decreases smoothly until it reaches its minimum value of 6.5 for frequencies up to 13 MHz. This value found for low frequencies is slightly below those reported for  $\text{BaTiO}_3$  based composites [24]. Furthermore, the dielectric constant at high frequencies is close to the expected value for extrinsic semiconductors [25]. Meanwhile, the obtained result for the dielectric constant is affected by the nonuniform polycrystalline character with respect to the sizes and shapes of the grains, and the not completely densified distribution of the samples, so that the influence of the grain limits the macroscopic response.

The measurements of resistivity as a function of temperature are shown in Fig. 6a. The observed behavior is clearly exponential, as expected in materials in which thermally activated electrical transport processes take place. An adjustment following an Arrhenius-type behavior was carried out, as shown in the inset of Fig. 6, where it is observed that the resistive response has the characteristics given by [26]

$$\rho(T) = \rho_0 e^{\left(\frac{T_0}{T}\right)^{1/n}}, \quad (2)$$

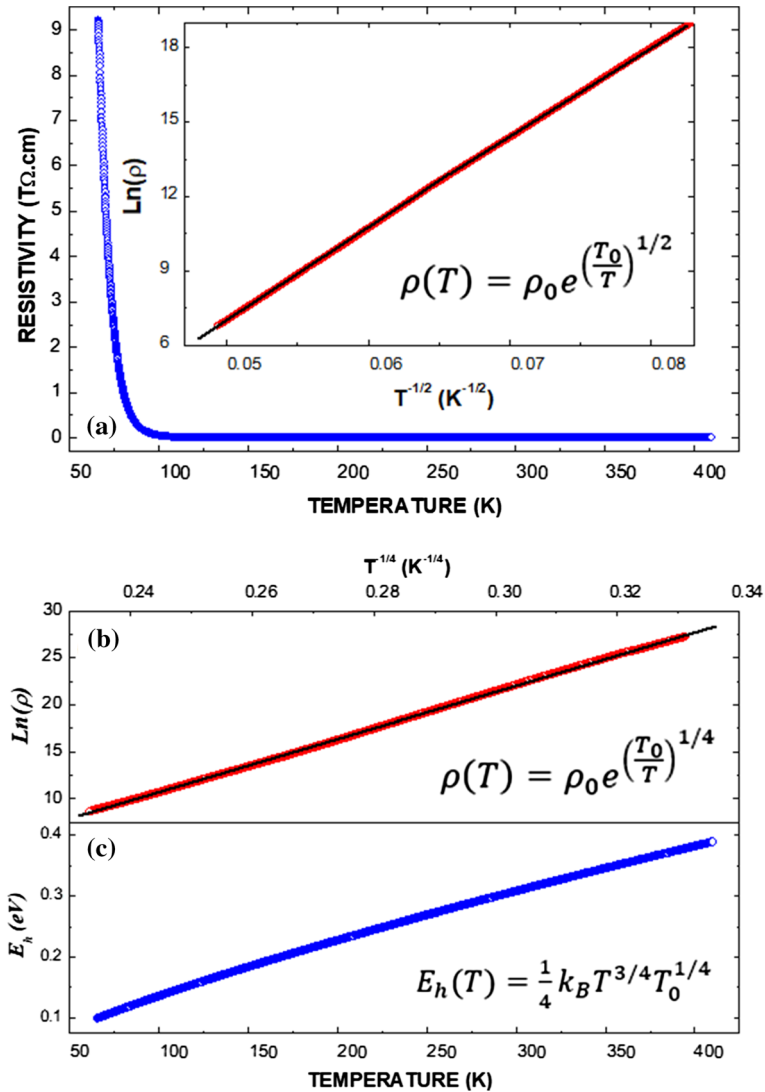


**Fig. 6** **a** Resistivity as a function of temperature measured in the  $\text{Nd}_{2.68}\text{Sr}_{1.32}\text{Mn}_{1.2}\text{Ti}_{1.32}\text{Fe}_{1.48}\text{O}_{12}$  samples. The inset represents the high-temperature fitting with the Arrhenius behavior for  $n=1/2$ . **b** Low-temperature fitting for  $n=1/4$ . **c** hopping energy behavior (Color figure online)

where  $\rho_0$  represents the pre-exponential resistive factor,  $n$  has integer values 2, 3 or 4, depending on dimensionality and specific temperature regime,  $k_B$  is the Boltzmann constant and

$$T_0 \sim \frac{18}{k_B N(E_F)} \tag{3}$$

is the percolation characteristic temperature, which can be expressed in terms of the density of states close to the Fermi energy,  $N(E_F)$  [26]. As shown in Fig. 6b, the best fit obtained in the regime of  $T < 250$  K corresponds to  $n=4$  with variable hopping energy that can be obtained as a function of the temperature from the expression

$$E_h(T) = \frac{1}{4} k_B T^{3/4} T_0^{1/4}. \quad (4)$$

The transport mechanism associated with this behavior is known as Mott's variable-range hopping (VRH) model, which is very interesting in the semiconductor industry because it facilitates the application of layer-type devices instead of single crystals [27]. As shown in the inset of Fig. 6a, in the region of high temperatures ( $250 \text{ K} < T < 410 \text{ K}$ ), the best fit took place for  $n=2$ , suggesting a mechanism of conduction of hopping of small polarons, known as Efros–Shklovskii type (ES), which is a model where the occurrence of a Coulomb gap is considered, which can be idealized as small jumps in the density of states close to the Fermi level, caused by interactions between localized electrons [28]. An eventual crystalline field splitting due to the cations  $\text{Mn-}3d^5$  and  $\text{Fe-}3d^6$ , which has no place for  $\text{Ti-}3d^2$  when the B cation of the perovskite structure is occupied by  $\text{Ti}^{4+}$ , together with the natural cationic disorder due to the unequal stoichiometric proportions of these cations in the material, and which is indistinguishable from the structural analysis, as well as the randomness of the octahedral distortions, could hinder the hybridizations between some electronic orbitals in the vicinity of the Fermi level, giving rise to delocalized charge carriers that would be responsible for the resistive behavior at high temperatures [29]. From the linear fit of Fig. 6b, the parameter  $\rho_0 = 3.356 \times 10^{-17} \Omega \cdot \text{cm}$  was obtained.

Figure 6c represents the behavior of the hopping energy obtained through Eq. (4). A decrease in the hopping energy from 0.38802 to 0.09968 eV is observed when the temperature decreases from 410 to 67 K. This result allows us to affirm that the decrease in temperature (associated with a consequent decrease in the number of phonons) also decreases the energy. For this reason, at low temperatures the VRH transport mechanism would take place, where the electronic states located close to the Fermi level do not transport charge at the thermodynamic limit, so that the electrical transport is aided by phonons to reach sites of favorable energy proximity.

### 3.3 Optical Band Gap

The previous results indicate that the  $\text{Nd}_{2.68}\text{Sr}_{1.32}\text{Mn}_{1.2}\text{Ti}_{1.32}\text{Fe}_{1.48}\text{O}_{12}$  material behaves like a varistor, which is why it is interesting to obtain the value of the band gap. The technique used for this purpose was diffuse reflectance spectroscopy in the frequency range from ultraviolet to near infrared, as shown in Fig. 7a, where three well-defined wavelength regimes are observed, which have been labeled as  $\lambda_1 = 345 \text{ nm}$ ,  $\lambda_2 = 980 \text{ nm}$  and  $1604 \text{ nm} < \lambda_3 < 1620 \text{ nm}$ . These three regimes, corresponding to the energies 3.6 eV, 1.27 eV and 0.77 eV  $< E < 1.03$  eV, are related to transition mechanisms of carriers between the valence and the conduction bands.

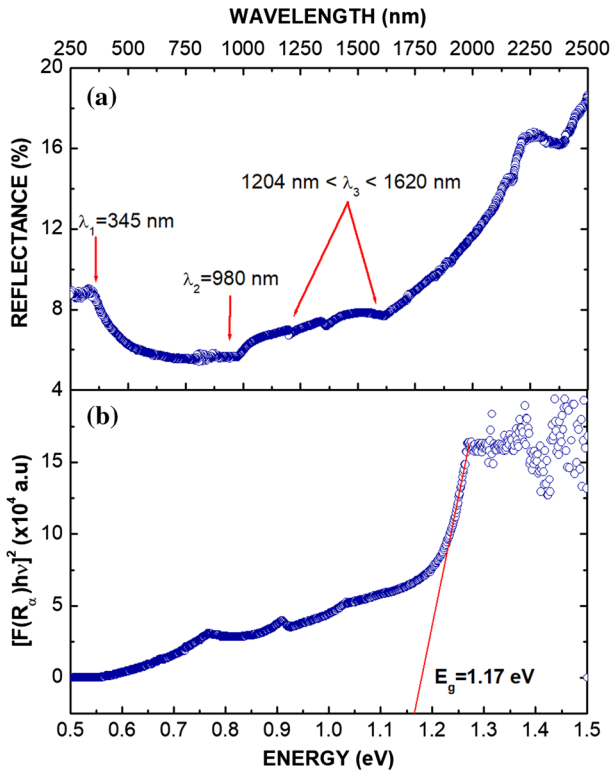


**Fig. 7** Diffuse reflectance result **a** and analysis of the experimental data for the determination of the optical band gap through the Tauc equation **b** for the  $\text{Nd}_{2.68}\text{Sr}_{1.32}\text{Mn}_{1.2}\text{Ti}_{1.32}\text{Fe}_{1.48}\text{O}_{12}$  material (Color figure online)

Meanwhile, these excitations have to do with structural symmetry [30]; therefore, for the  $\text{Nd}_{2.68}\text{Sr}_{1.32}\text{Mn}_{1.2}\text{Ti}_{1.32}\text{Fe}_{1.48}\text{O}_{12}$  complex perovskite, the appearance of these three energy regions in the DRS spectrum is due to the occurrence of vibrations in the bonds  $\text{O}2p\text{-Nd}5d$ ,  $\text{O}2p\text{-Sr}5s$ ,  $\text{O}2p\text{-Mn}3d$ ,  $\text{O}2p\text{-Ti}3d$  and  $\text{O}2p\text{-Fe}3d$ .

Due to the above, the lowest energy regimen  $0.77 \text{ eV} < E < 1.03 \text{ eV}$  shows three small anomalies, showing that for the DRS technique there is no indistinguishability between the Nd and Sr cations at sites A and between the Mn, Ti and Fe cations in the B sites of the generic structure  $\text{A}_{4-x}\text{A}'_x\text{B}_{4-y-z}\text{B}'_y\text{B}''_z\text{O}_{12}$ . On the other hand, the excitations of the three energy regimes mentioned above agree with the irreducible representation for vibrations:

$$\Gamma = 5_{\text{RSM}} + 7\text{B}1\text{u} + 9\text{B}2\text{u} + 9\text{B}3\text{u}, \quad (5)$$

where the first term represents five modes of vibration that cannot be observed by DRS but by means of Raman spectroscopy, while the modes  $7\text{B}1\text{u} + 9\text{B}2\text{u} + 9\text{B}3\text{u}$  correspond to the three regions previously determined in the UV–Vis–NIR spectrum [31]. Based on the results, the appropriate analysis method for determining the band

gap was Kubelka–Munk, which was applied as proposed by V. Kumar et al. [32] as shown in Fig. 7b. Meanwhile, it is necessary to consider that in a polycrystalline material with the morphology discussed in Sect. 3.1, inhomogeneities must be taken into account within the value of  $E_g$ , which must be considered as a macroscopic average that contains gap values less than  $E_g$  due to the charge carriers supplied by the grain boundaries perpendicular to the direction of the current, values greater than  $E_g$  due to the insulating grain boundaries and the potential due to the porous feature of the samples ( $V_p > E_g$ ). The band gap obtained for the perovskite under study was  $E_g = 1.17$  eV, which is characteristic of a good semiconductor material with direct band gap and whose value is equal to that observed in InGaAs/GaAsP multiple quantum wells, where the number of unions favors the greater efficiency [33], and in perovskite/silicon tandem [34], making it applicable in the new semiconductor technology.

### 3.4 Magnetic Susceptibility and Magnetization

Measurements of magnetic susceptibility as a function of temperature between 50 and 325 K for an external field  $H = 500$  Oe were performed to determine the magnetic feature of the  $\text{Nd}_{2.68}\text{Sr}_{1.32}\text{Mn}_{1.2}\text{Ti}_{1.32}\text{Fe}_{1.48}\text{O}_{12}$  material, as exemplified in Fig. 8. The resulting curves show the occurrence of irreversibility between the ZFC and FC measurement procedures. In the first, the magnetic moment system is frozen before the application of the external field, measuring during the sample heating process, while in the second, the measurement is carried out while the temperature is decreased in the presence of applied field intensity. This type of behavior like that of spin glasses is characteristic of perovskite-type

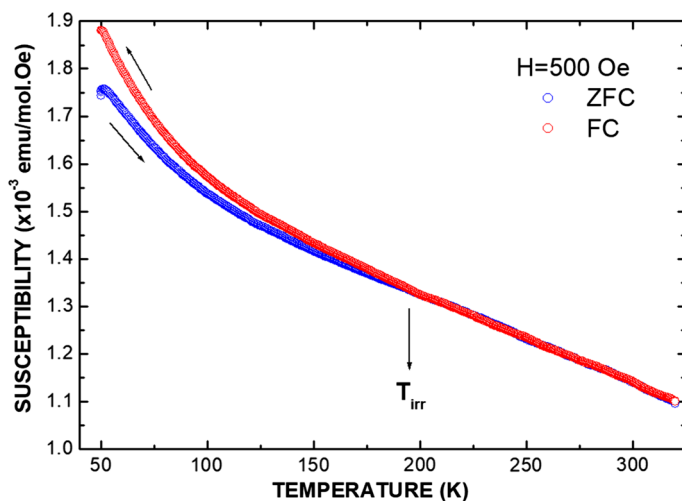


**Fig. 8** Temperature dependence of the magnetic susceptibility for the  $\text{Nd}_{2.68}\text{Sr}_{1.32}\text{Mn}_{1.2}\text{Ti}_{1.32}\text{Fe}_{1.48}\text{O}_{12}$  samples (Color figure online)

ferromagnetic materials and takes place due to the structural disorder of the cations that contribute spins to the conformation of the magnetic domains [35].

In the case of the material under study, the structural analysis showed that there is no ordering of the Nd and Sr cations in the structural sites A and of the Mn, Ti and Fe cations in the B sites of the cell along the crystallographic axes, which creates the appropriate environment for the appearance of the type of magnetocrystalline anisotropy that gives rise to irreversible behavior. Similarly, the octahedral distortions produce a canting effect of the spins of the magnetic cations, modifying the correlation potentials between the domains, thus hindering a collective response of all the magnetic moments during the ZFC measurement recipe. Additional contributions to the magnetic anisotropy are due to the granular inhomogeneity observed in Fig. 3, as discussed above.

Then, measurements of magnetization as a function of the applied magnetic field were carried out as shown in Fig. 9 for fixed temperature values of 50, 200 and 300 K, in the field intensity regimes of  $-8.0 \text{ kOe} < H < 8.0 \text{ kOe}$ . For all temperature values, the hysterical behavior typical of materials with magnetic ordering is observed. The material is classified as ferromagnetic, with characteristic parameters presented in Table 3, with small values of coercive fields ( $H_C$ ), remnant magnetization ( $M_R$ ) and apparent saturation magnetizations ( $M_S$ ). Meanwhile, the temperature regime evaluated did not allow to establish the value of the Curie temperature  $T_C$ , which must be above 325 K, which can be stated due to the occurrence of hysteresis at room temperature in Fig. 9 and the smoothness of the susceptibility curve (Fig. 8), since, in  $T_C$ , the expected transition in ferromagnetic materials is of second order, with which, due to Curie's law, an abrupt fall with subsequent dependence of the susceptibility with the inverse of  $T - T_C$  was observed.

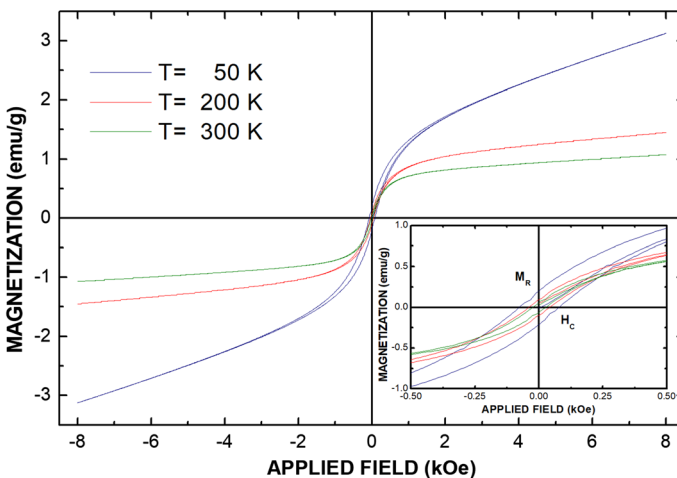


**Fig. 9** Magnetic ordering in hysteretic curves of the magnetization as a function of applied fields for the  $\text{Nd}_{2.68}\text{Sr}_{1.32}\text{Mn}_{1.2}\text{Ti}_{1.32}\text{Fe}_{1.48}\text{O}_{12}$  perovskite at temperature values of 50 K, 200 K and 300 K. A magnification of the magnetic field regime close to  $H \approx 0$  is presented in the inset of figure (Color figure online)

**Table 3** Magnetic parameters for the  $\text{Nd}_{2.68}\text{Sr}_{1.32}\text{Mn}_{1.2}\text{Ti}_{1.32}\text{Fe}_{1.48}\text{O}_{12}$  complex perovskite

$T$ (K)	$H_C$ (Oe)	$M_R$ ( $\pm 0.001$ emu/g)	$M_S$ ( $\pm 0.001$ emu/g)
50	82.7	0.211	1.39
200	49.1	0.098	0.95
300	24.9	0.045	0.79

The ferromagnetic character of the material at room temperature, together with the semiconductor nature of perovskite  $\text{Nd}_{2.68}\text{Sr}_{1.32}\text{Mn}_{1.2}\text{Ti}_{1.32}\text{Fe}_{1.48}\text{O}_{12}$ , allows its classification as an advanced functional material, also suggesting its eventual application in spintronic devices.

## 4 Conclusions

The  $\text{Nd}_{2.68}\text{Sr}_{1.32}\text{Mn}_{1.2}\text{Ti}_{1.32}\text{Fe}_{1.48}\text{O}_{12}$  material was produced through the solid-state reaction method. The structural characterization was carried out by means of X-ray diffraction. The results of the Rietveld refinement of the experimental data allowed us to conclude that this material adopts a nonsymmetric perovskite-type orthorhombic structure, with strong evidence of octahedral distortion, which belongs to the space group Pnma. The morphological study using SEM images revealed the formation of grains with relatively strong coupling to each other, with diverse shapes and with micrometric granular sizes (1.50  $\mu\text{m}$ ). EDS spectroscopy revealed the lack of chemical phases not corresponding to the proposed stoichiometric formula. The characteristic of the E–J electrical response is in accordance with a varistor-type behavior, which takes place due to the competition between the inter- and intra-granular resistive effects. The figure of merit of the equivalent varistor results in a nonlinear coefficient  $\alpha = 1.03$ , which is attributed to the quasi-metallic behavior at low current densities, which adopts a completely nonlinear trend for high currents, as a consequence of the semiconductor microjunctions of grains coupled by morphological inhomogeneities. From the resistivity curve as a function of temperature, it was established that in the low-temperature regime, a transport mechanism of the Mott's variable-range hopping type assisted by phonons predominates, while at high temperatures the transport of charge carriers is of the hopping of small polarons type (Efros–Shklovskii). DRS UV–Vis–NIR spectra revealed the occurrence of three vibration regimes related to cation–anion bonds within the unit cell. The Kubelka–Munk analysis showed an optical band of 1.17 eV, which allows establishing the semiconductor character of this material. Measurements of the magnetic response of the material in susceptibility curves as a function of temperature suggest a ferrimagnetic-type behavior. Magnetic anisotropies due to structural distortions and cationic disorder produce irreversibility effects between the curves measured by the ZFC and FC procedures. Similarly, the granular nature of the material is also likely to give rise to mechanisms that hinder correlation between magnetic moments, increasing the anisotropic character of the magnetic response at low temperatures.

Finally, the magnetization curves as a function of the applied field showed a hysterical behavior, which is characteristic of materials in which the order of the spins is due to the occurrence of magnetic domains. Meanwhile, the observed values for coercive field, remaining magnetization and saturation magnetization are very small, suggesting that the application of weak bias magnetic field intensities can reverse the magnetization state of the system. These results, together with the semiconductor nature of the material, bode well for the potential applicability of the material in spintronic devices that require rapid manipulation of the magnetic moment.

**Acknowledgements** This work was partially supported by Division of Investigation and Extension (DIEB) of the National University of Colombia and MINCIENCIAS, on the project FP80740-243-2019. First author, J.A Cuervo Farfán, received support by MINCIENCIAS on the scholarship program for national Ph.D. students.

## References

1. S. Bhatti, R. Sbiaa, A. Hirohata, H. Ohno, S. Fukami, S.N. Piramanayagam, *Mater. Today* **20**, 530 (2001)
2. E.L. Nagaev, *Phys. Rep.* **346**, 387 (2001)
3. B. Raveau, A. Maignan, C. Martin, M. Hervieu, *Chem. Mater.* **10**, 2641 (1998)
4. C.J. Howard, B.J. Kennedy, P.M. Woodward, *Acta Cryst. B* **59**, 463 (2003)
5. C.A. Triana, D.A. Landínez Téllez, J. Roa-Rojas, *Mater. Character.* **99**, 128 (2015)
6. C.A. Triana, D.A. Landínez Téllez, J. Roa-Rojas, *J. All. Compnd.* **516**, 179 (2012)
7. Y. Shimakawa, *Inorg. Chem.* **47**, 8562 (2008)
8. J.A. Cuervo Farfán, C.A. Parra Vargas, D.S.F. Viana, F.P. Milton, D. Garcia, D.A. Landínez Téllez, J. Roa-Rojas, *J. Mater. Sci.: Mater. Electron.* **29**, 20942 (2018)
9. D.P. Llamasa, D.A. Landínez Téllez, J. Roa-Rojas, *Phys. B.: Cond. Mat.* **404**, 2726 (2009)
10. S.J. Yuan, W. Ren, F. Hong, Y.B. Wang, J.C. Zhang, L. Bellaiche, S.X. Cao, G. Cao, *Phys. Rev. B* **87**, 184405 (2013)
11. K.F. Wang, J.-M. Liu, Z.F. Ren, *Adv. Phys.* **58**, 321 (2009)
12. L.C. Moreno, J.S. Valencia, D.A. Landínez Téllez, J. Arbey Rodríguez, M.L. Martínez, J. Roa-Rojas, F. Fajardo, *J. Magn. Magn. Mater.* **320**, 19 (2008)
13. T. Chatterji, P.F. Henry, B. Ouladdiaf, *Phys. Rev. B* **77**, 212403 (2008)
14. P.E. Tomaszewski, N. Miniajluk, M. Zawadzki, J. Trawczyński, *Phase Transit.* **92**, 525 (2019)
15. H.E. Weaver, *J. Phys. Chem. Solids* **11**, 274 (1959)
16. K.M. Ginell, C. Horn, R.B. Von Dreele, B.H. Toby, *Powder Diffr.* **34**, 184 (2019)
17. E. Parthé, L. Gelato, B. Chabot, M. Penzo, K. Cenzual, R. Gladyshevskii, (1993) TYPIX Standardized and crystal chemical characterization of inorganic structure types. In: Gmelin Handbook of Inorganic and Organometallic Chemistry 8th ed. Springer, Berlin.
18. C.A. Schneider, W.S. Rasband, K.W. Eliceiri, *Nat. Methods* **9**, 671 (2012)
19. G. Blatter, F. Greuter, *Phys. Rev. B* **33**, 3952 (1986)
20. H. Bidadi, S. Hasanli, M. Hekmatshoar, S. Bidadi, S. Mohammadi Aref, *Vacuum* **84**, 1232 (2010)
21. A. Vojta, Q. Wen, D.R. Clarke, *Comp. Mater. Sci.* **6**, 51 (1996)
22. R.K. Pandey, W.A. Stapleton, I. Sutanto, *J. Electron. Device. Soc.* **3**, 273 (2015)
23. M. Matsuoka, *Japan. J. Appl. Phys.* **10**, 736 (1971)
24. A. Zed, S.J. Milne, *J. Mater. Sci. Mater. Electron.* **26**, 9243 (2015)
25. J. Singh, *Semiconductor Physics and Its Heterostructures*. Mcgraw Hill Series in Electrical and Computer Engineering, New York, (1993).
26. P.V.E. McClintock, D.J. Meredith, J.K. Wigmore. *Matter at Low Temperatures*. Blackie. 1984 ISBN 0-216-91594-5.
27. M. Affronte, M. Campani, S. Piccinini, M. Tamborin, B. Morten, M. Prudenziati, *J. Low Temp. Phys.* **109**, 461 (1997)
28. A.L. Efros, B.I. Shklovskii, *J. Phys. C: Sol. Stat. Phys.* **8**, L49 (1975)



29. S. Kurth, M.A.L. Marques, E.K.U. Gross, in *Encyclopedia of Condensed Matter Physics*, Ed. by F. Bassani, J. Liedl, P. Wyder, (Elsevier, Amsterdam, 2005), pp. 395–402
30. J.A. Cuervo Farfán, D.M. Aljure García, R. Cardona, J. Arbey Rodríguez, D.A. Landínez Téllez, J. Roa-Rojas, *J. Low Temp. Phys.* **186**, 295 (2017)
31. M. Sorescu, T. Xu, A. Hannan, *J. Mater. Sci. Technol.* **1**, 57 (2011)
32. V. Kumar, S. Kr Sharma, T.P. Sharma, V. Singh, *Opt. Mater.* **12**, 115 (1999)
33. K. Toprasertpong, H. Fujii, T. Thomas, M. Führer, D. Alonso-Álvarez, D.J. Farrell, K. Watanabe, Y. Okada, N.J. Ekins-Daukes, M. Sugiyama, Y. Nakano, *Prog. Photovolt. Res. Appl.* **24**, 533 (2016)
34. M. Hossain, W. Ma, S. Qarony, L. Zeng, D. Knipp, Y.H. Tsang, *Nano-Micro. Lett.* **11**, 58 (2019)
35. R.L. Falge Jr., N.M. Wolcott, *J. Low Temp. Phys.* **5**, 617 (1971)

**Publisher's Note** Springer Nature remains neutral with regard to jurisdictional claims in published maps and institutional affiliations.